JGR Solid Earth

RESEARCH ARTICLE
10.1029/2022JB025040

Special Section:
Understanding and anticipating Induced Seismicity: from mechanics to seismology

# Influence of Fault Architecture on Induced Earthquake Sequence Evolution Revealed by High-Resolution Focal Mechanism Solutions

**Yan Qin[1], Xiaowei Chen[2,3], Ting Chen[1], and Rachel E. Abercrombie[4]**

[1]Earth and Environmental Sciences Division—Geophysics Group, Los Alamos National Laboratory, Los Alamos, NM, USA, [2]School of Geosciences, University of Oklahoma, Norman, OK, USA, [3]Department of Geology and Geophysics, Texas A&M, College Station, TX, USA, [4]Department of Earth and Environment, Boston University, Boston, MA, USA

**Abstract** The increasing seismicity and improved seismic observation network in recent years provide an opportunity to explore factors that influence the triggering processes, spatiotemporal evolution, and maximum magnitude of induced sequences. We map the fault architecture and stress state of four induced sequences in Oklahoma to determine their influence on the seismicity. We systematically relocate the earthquakes and compute hundreds of focal mechanisms of small to medium events ($1.0 < M < 5.1$) using various techniques, including machine learning, for the Guthrie, Woodward, Cushing, and Fairview sequences. The detailed fault geometry and spatiotemporal evolution of seismicity and stress states reveal different dominant driving forces for each sequence. In Cushing and Fairview (largest event ≥M5.0), the main fault structures are near-vertical narrow strike-slip faults, with most of the small earthquake fault planes optimally oriented. The two sequences exhibit discontinuous temporal migration but strong earthquake self-driven rupture growth. In Guthrie and Woodward (largest event <M5.0), the two sequences show more complex diffuse fault structures with varying dipping angles along depth. The inverted focal mechanisms show a mix of strike-slip faulting and normal faulting in both sequences, and the normal faulting events are less optimally oriented than strike-slip events. The two sequences are dominated by continuous diffusive migration in time driven by pore pressure propagation. The above results suggest that fault architecture and stress state influence sequence evolution, major driving forces, and possibly maximum magnitude.

**Plain Language Summary** Oklahoma has experienced a drastic increase of earthquakes due to waste-water injection in the last decades, which provides data to study the physical causes of induced earthquakes. The maximum magnitude of the triggered earthquakes varies in different sequences on account of the fault structures. We use geophysical methods to obtain the precise location and detailed fault orientations of the earthquakes. Then using geomechanical analysis, we could determine if the fault plane of an earthquake is close to failure in the ambient stress field. We analyze four earthquake sequences—Guthrie, Woodward, Cushing, and Fairview in Oklahoma using the above methods. We find that for sequences with simpler fault structures like Cushing and Fairview, more earthquakes are close to failure, the driving force of the sequence is mainly earthquake interaction (large earthquakes triggering small earthquakes), and the largest magnitudes are above 5.0. For sequences with complex mesh fault structures like Guthrie and Woodward, fewer earthquakes are close to failure, the driving force of the sequence is fluid diffusion from injection, and the largest magnitudes are smaller than 5.0. Our findings suggest that fault architecture and stress state influence sequence evolution and are critical to evaluate induced earthquake hazards.

**Key Points:**

- Faults with $M \geq 5$ earthquakes (Fairview/Cushing) tend to be vertical strike-slip faults with mostly optimally oriented individual events
- Faults with smaller earthquakes (Guthrie/Woodward) show a mixture of strike-slip and normal faults with fault mesh networks
- Fault structures control the induced earthquake sequence evolution in Oklahoma

**Supporting Information:**

Supporting Information may be found in the online version of this article.

**Correspondence to:**

Y. Qin,
yan.qin-1@ou.edu

**Citation:**

Qin, Y., Chen, X., Chen, T., & Abercrombie, R. E. (2022). Influence of fault architecture on induced earthquake sequence evolution revealed by high-resolution focal mechanism solutions. *Journal of Geophysical Research: Solid Earth*, *127*, e2022JB025040. https://doi.org/10.1029/2022JB025040

Received 27 JUN 2022
Accepted 27 OCT 2022

**Author Contributions:**

**Formal analysis:** Yan Qin
**Funding acquisition:** Xiaowei Chen, Ting Chen
**Methodology:** Yan Qin, Xiaowei Chen
**Supervision:** Xiaowei Chen, Ting Chen



## 1. Introduction

The seismicity rate in Oklahoma has experienced significant variations during the last decades, which has been mostly attributed to wastewater disposal (e.g., Ellsworth, 2013; Keranen et al., 2014; Yeck et al., 2016). With the improved monitoring network in Oklahoma, high-resolution seismicity relocations have revealed previously unknown fault structures and rupture processes. For example, Schoenball and Ellsworth (2017a), Qin et al. (2019), and Skoumal et al. (2019) systematically mapped seismogenic faults through relocated seismicity in Oklahoma. At local scale, fault networks and the potential driving mechanisms have been studied for individual sequences, for example, in Prague (e.g., Keranen et al., 2013), Pawnee (Chen et al., 2017; Pennington & Chen, 2017), Guthrie-Langston (Schoenball et al., 2018), Guthrie (e.g., Chen et al., 2018; Pennington et al., 2022;

**Visualization:** Rachel E. Abercrombie
**Writing – review & editing:** Xiaowei Chen, Ting Chen, Rachel E. Abercrombie

Wu et al., 2019), Fairview (e.g., Goebel et al., 2017; McGarr & Barbour, 2017; Yeck et al., 2016), and Woodward (Qin et al., 2018).

Although these sequences are all related to wastewater disposal, their fault structures and sequence evolution exhibit significant differences. For example, two recent studies showed sequences with maximum magnitude ($M_{max}$) around four involved mixed normal and strike-slip faulting and were dominated by swarm-like activity. Chen et al. (2018) showed that the Guthrie sequence in central Oklahoma, with maximum magnitude of 4.0, had a mixture of normal and strike-slip faulting and followed clear diffusive migration. In Woodward, Qin et al. (2018) mapped a complex flower structure with a mix of strike-slip and normal faulting events, and the seismicity migration pattern followed the pore pressure and poroelastic stress changes (Goebel et al., 2017). However, the $M \geq 5$ sequences in Oklahoma are mostly dominated by strike-slip faulting mechanism and have clear aftershock sequences with stress interactions (Chen et al., 2017; Keranen et al., 2013). Qin et al. (2019) noted that the four $M \geq 5$ earthquakes in Oklahoma all occurred along faults that were optimally oriented, and for sequences that were less optimally oriented, the largest magnitude was usually less than 4. These observations suggest that the fault characteristics could influence the sequence evolution and major driving forces.

Resolving detailed fault architecture and evolution of the stress state requires both high-resolution earthquake relocations and focal mechanisms. However, constraining the focal mechanism of small earthquakes remains difficult because of the low signal-to-noise ratio (SNR) and a lack of azimuthal coverage in many areas. New techniques have been developed to improve focal mechanism determinations and uncertainty characterization. Vavryčuk (2015) inverted for a composite moment tensor using joint inversion of multiple earthquake data. Pugh et al. (2016) and De Matteis et al. (2016) inverted moment tensor from various inputs using Bayesian frameworks. Spatially concentrated earthquakes, such as earthquake swarms and mainshock-aftershock sequences, often show similar mechanisms. Shelly, Hardebeck, et al. (2016) developed a strategy for earthquake focal mechanism using waveform-correlation-derived relative polarities and clustering analysis. This strategy clustered events with similar patterns of polarities and applied focal mechanism inversion to the grouped polarity data. With the increasing application of machine learning methods in seismology, Ross et al. (2018) trained a convolutional neural network to pick first-motion polarities of *P* waveform and demonstrated that the model could pick polarities accurately.

Taking advantage of these new techniques in analyzing small earthquakes, we perform detailed analysis of four sequences with different temporal behaviors, aiming at better understanding of the factors that influence evolution of induced earthquake sequences and the major driving forces. The selected sequences include: the Guthrie and Woodward sequences that are more swarm-like with the largest magnitude of four or lower; the Cushing and Fairview sequences that have $M \geq 5$ events and aftershocks. For each of the sequence, we obtain high-resolution locations and focal mechanisms, which we use to map earthquake spatiotemporal migration, interpret fault architecture, and investigate the evolution of stress states. These results are then integrated to understand factors that lead to the different behaviors of these sequences.

## 2. Data

We use the earthquake catalog from the Oklahoma Geological Survey (OGS) from January 2009 to August 2018 (Walter et al., 2020). In the four sequences in Guthrie, Woodward, Cushing, and Fairview, there are 1,073, 1,404, 681, and 3,460 cataloged events with magnitude range from 0.1 to 5.1 (Figure 1). The catalog covers the onset, peak, and arrest of seismicity in each sequence. We perform relocation for four sequences by including some more recent events compared to previous studies. Also, relocating these sequences in the same manner ensures consistency for the interpretation.

For the waveform data, we select stations within 150 km of the sequence to ensure data quality in Cushing and Guthrie. For Woodward and Fairview, the distance cutoff is set to 250 km due to the lack of station coverage in northwest Oklahoma (Figure 1). We remove the linear trends of the waveform and then apply bandpass filtering (1–20 Hz). The processed waveforms are used in the following analysis.

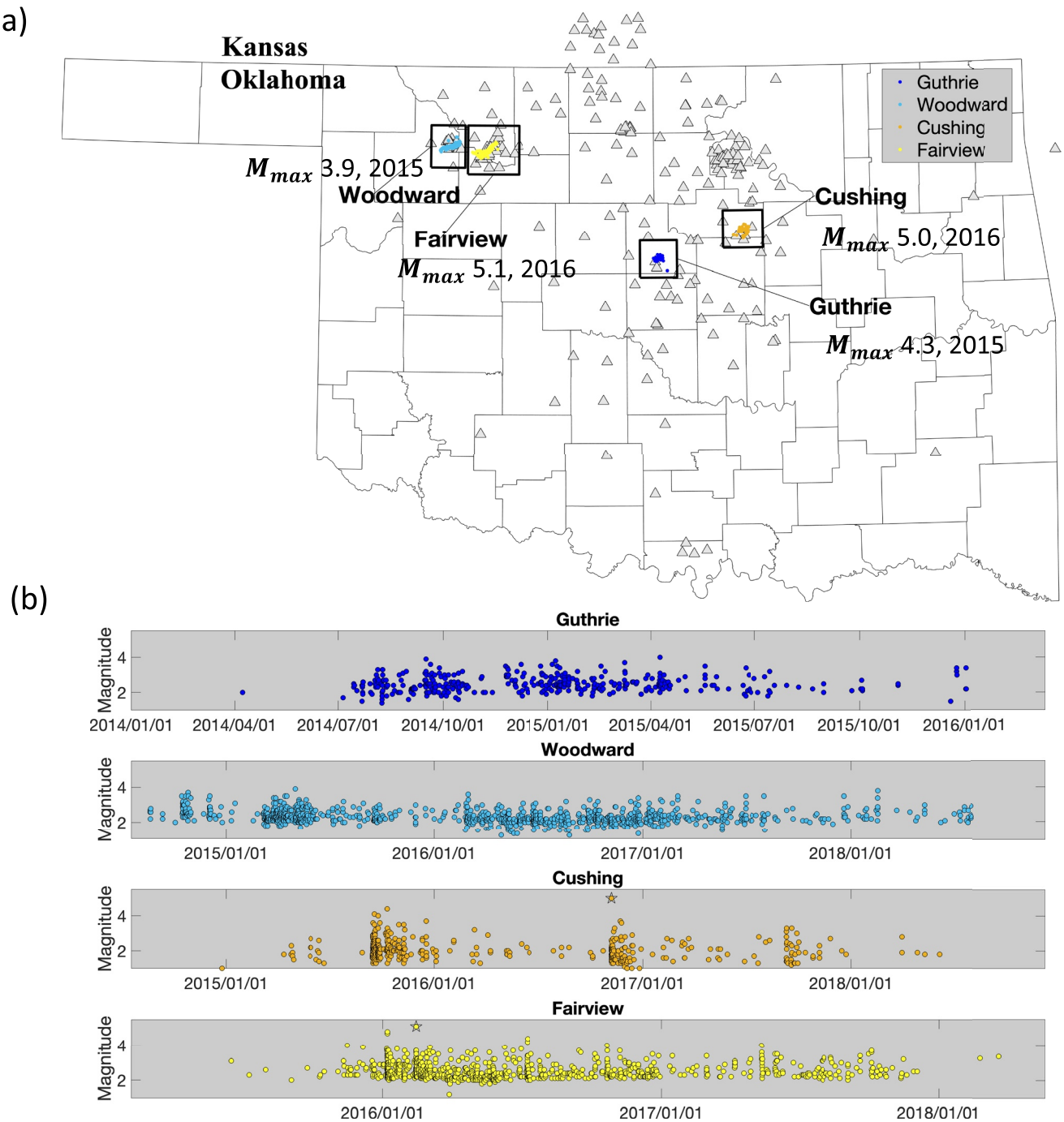


**Figure 1.** (a) Earthquake and station distributions. The gray triangles are seismic stations. The colored dots are earthquakes (2009–2018) for four sequences: Guthrie, Woodward, Cushing, and Fairview. (b) The magnitude-time distribution for four sequences. The M5 events in Cushing and Fairview sequences are highlighted by stars.

## 3. Method

### 3.1. Earthquake Relocation

We use hypoDD (Waldhauser, 2001) to compute earthquake relocations with the 1D velocity model from Darold et al. (2015). Differential travel times are calculated using both phase arrivals and cross correlations. We obtain *P* and *S* phase arrivals from OGS, and for events without available cataloged arrivals, we use an automated phase picker from Li and Peng (2016) to estimate *P* and *S* arrival times based on the 1D velocity model (Darold

et al., 2015). The phase arrivals are further refined in a pretrained machine learning model (Ross et al., 2018). For each earthquake, we store *P* and *S* phase arrivals for up to 20 closest neighboring earthquakes within a distance of 10 km. For each event pair, we store the differential travel times on all stations within 200 km.

To compute the differential time from cross correlations, we first use a time window of 1.5 s (0.5 s before and 1.0 s after the arrival on vertical channel) and 2.5 s (1 s before and 1.5 s after the arrival on horizontal channels) for *P* and *S* wave, respectively, to compute the cross-correlation coefficients. For the S wave, the channel with higher cross-correlation coefficient is selected to measure the differential travel time. We require a minimum cross-correlation coefficient of 0.7 and use the squared cross-correlation coefficient as its weight in the relocation procedure following Schoenball and Ellsworth (2017b).

In the first set of iterations of hypoDD, we give the differential travel times calculated from *P* and *S* phase picks the highest weight to constrain the overall geometry using all earthquakes. In later iterations, we add differential travel times measured from cross-correlation time lags and decrease the weight of the catalog picks. In the last step, we use only cross-correlation measurements to resolve the fine structures. We should point out that for the event relocations, the relative depth is more robust, and the absolute depth may be less reliable. Table S1 in Supporting Information S1 lists the relocation results.

### 3.2. Spatiotemporal Migration

The spatiotemporal evolution of sequences could reflect the relative importance of different driving forces. Here we use the following three parameters (migration pattern with time, migration pattern with event index, and the coefficient of variation of interevent delay time) to study the mechanisms of each sequence.

Following Haffener et al. (2018) and assuming homogeneous isotropic permeability of fault zones in each sequence, we model the diffusive migration ($r \sim \sqrt{(t)}$) for each sequence using weighted grid-search, where $t$ is the event elapsed time and $r$ is the 3D distance between event location and the starting location of migration (the average location of the earliest 5% of the total events). We estimate the statistical significance of diffusive migration with 100 resampled datasets where the event occurrence time is randomly shuffled.

Fischer and Hainzl (2021) argued that such temporal migration analysis for earthquake swarms assumed earthquakes were passively responding to external stress perturbations and that it ignored the interactions between rupture front and surrounding rock matrix (Yamashita, 1999). They proposed that for sequences with disruptive temporal migration, an examination of rupture growth with event index (regarded as natural time of earthquake occurrence) ($r \sim \sqrt{(N)}$) was also needed. So, we also plot this for the four sequences we study.

Schoenball and Ellsworth (2017a) has found that seismic diffusivity is positively correlated with the coefficient of variation ($C_v$) of event delay time. The $C_v$ is defined as,

$$C_v(dt) = \sigma_{dt}/\bar{dt} \tag{1}$$

where $\sigma_{dt}$ and $\bar{dt}$ are the standard deviation and the mean of interevent delay time $dt$. The $C_v$ value is 0 for periodic events, 1 for exponentially distributed interevent times (Poisson process), and higher than 1 for temporally clustered occurrence times. Stronger temporal clustering indicates earthquake interactions.

### 3.3. Focal Mechanisms

#### 3.3.1. *P* Wave Polarity

Picking the first-motion polarities for small earthquakes is difficult due to the low SNR. Here, we select two methods, waveform-correlation-derived relative polarities (hereinafter referred to as SVD method) (Shelly, Hardebeck, et al., 2016) and a pretrained deep learning model for polarity classification (referred to as ML method) (Ross et al., 2018). The results from the two methods are then compared and combined to invert for focal mechanisms using hybridMT (Kwiatek et al., 2016).

**Table 1**
*Polarity Result Comparison for SVD and ML Methods*

| Sequence | Templates | SVD Pols | ML Pols | Consist | Inconsist | Consist rate |
|---|---|---|---|---|---|---|
| Guthrie | 2,466 | 9,954 | 14,008 | 8,336 | 168 | 98.02% |
| Woodward | 4,024 | 8,638 | 13,682 | 4,959 | 67 | 98.67% |
| Cushing | 2,807 | 9,031 | 12,212 | 7,025 | 178 | 97.53% |
| Fairview | 4,915 | 12,301 | 26,065 | 9,864 | 321 | 96.85% |

#### 3.3.1.1. SVD Method

We follow the method from Shelly, Hardebeck, et al. (2016) to derive *P* wave polarities for a whole sequence based on a small number of selected templates with known polarities. For each sequence, we randomly select around 100 events as templates and manually pick their polarities. Then we compare the similarity between all events and templates by computing the weighted relative polarity (defined by the absolute difference between the peak and the secondary peak of cross correlations multiplied by the sign of the peak correlation). Then the similarity matrix is reduced to a vector by taking the left singular vector of the left unitary matrix of its Singular Value Decomposition (SVD). This vector represents the SVD-derived polarity pattern of all events. We check the consistency between SVD-derived polarities and manually picked polarities for the selected templates to get a consistency factor. The SVD-derived polarities are then multiplied by the consistency factor to get the real polarity for a particular channel.

To control the quality of the results, we apply a cross-correlation coefficient cutoff of 0.8 and search for a cutoff value for SVD results by requiring that 98% of the derived polarities for templates are consistent with the manually picked polarities. The results are shown in Table 1.

#### 3.3.1.2. ML Method

In the second method, we use the pretrained convolutional neural network (CNN) model from Ross et al. (2018) to pick the polarities. The model was trained by over 2 million analyst-picked polarities of earthquakes in California. We apply the same preprocessing to the waveform data as in Ross et al. (2018), that is, the waveform is resampled to 100 Hz, detrended, and filtered between 1 and 20 Hz. Then we select a 4-s-long window centered on the *P* arrival time and normalize the waveform by the peak absolute amplitude in the window. The CNN model takes the 400-point time series as input and predicts the *P* polarities (up, down, or unknown). The results are evaluated using the metric of precision for each class of polarity (up and down). For a given class, the precision is defined as the number of true positives divided by the total number of records assigned to the class by the CNN model:

$$precison_u = \frac{TP_{uu}}{TP_{uu} + \epsilon_{du}}$$
$$precison_d = \frac{TP_{dd}}{TP_{dd} + \epsilon_{ud}} \quad (2)$$

where $u$ and $d$ represent polarity up and down, $TP$ is the number of true positives, and $\epsilon$ is the number of false positives. We test the model on template events in the four sequences. We iteratively search for an epicentral distance cutoff and a SNR (the ratio between the peak absolute amplitude in the 0.5 s after and before the phase arrival time) cutoff to ensure that the precision of template predictions is over 98% (Figure S1 in Supporting Information S1). The results are also shown in Table 1. Without any adjustment of the machine learning model, the prediction accuracy is comparable to the results reported in Ross et al. (2018). The successful application of the model to earthquakes in Oklahoma suggests good generalization of the model. We then apply the model to all events (epicentral distance <130 km and SNR ≥5) in the four selected sequences.

We compare the polarity picking results from SVD and ML methods and find that over 96% of the common events have consistent polarities (Table 1). The SVD method is most applicable to events with similar waveform to the templates, and the ML model can be applied to events with more complex sources. We combine the polarity results from the two methods for focal mechanism inversion. For a small fraction of inconsistent results, we choose the prediction results from the ML methods.

### 3.3.2. Focal Mechanism and Fault Architecture

We compute the earthquake focal mechanism solutions using the combined polarity results above in hybridMT (Kwiatek et al., 2016). To ensure the quality of the inversion, we select only events with a minimum of eight polarities, maximum azimuthal gap of 100°, and maximum takeoff angle gap of 60°. As shown in Figure S2 in Supporting Information S1, the median number of polarities is 40, 21, 32, and 29 for Guthrie, Woodward, Cushing, and Fairview, respectively. Since we only use polarity information and do not include the amplitude in the input data sets, the inverted full moment tensor may not be well constrained. So, we select double-couple

**Table 2**
*Quality Characterization Results of Inverted Focal Mechanisms*

| Sequence | A | B | C | D | Total |
|---|---|---|---|---|---|
| Guthrie | 20 | 101 | 63 | 125 | 309 |
| Woodward | 71 | 66 | 160 | 159 | 456 |
| Cushing | 115 | 69 | 38 | 49 | 271 |
| Fairview | 230 | 184 | 89 | 98 | 601 |

(DC) component of the moment tensor for the following analysis. The focal mechanisms are then categorized into strike-slip, normal, and reverse events based on the relative orientation of *P*/*T*/*B* axes (i.e., which axis is closer to the vertical).

We also use the input data resampling technique to assess the uncertainty of the moment tensor inversion. We assume 10% of input phases have wrongly picked polarity and add 10% random error to the velocity model (Figure S3 in Supporting Information S1). Then we resample the input data 100 times by randomly flipping the polarity of the input phase data. For each resampled input data set, we invert a different set of focal mechanisms. Based on the stability of inversion results from resampling, we use similar criteria as in HASH program (Hardebeck & Shearer, 2008) to assign the quality of the inverted focal mechanisms. A detailed quality assignment is listed in the Table S1 in Supporting Information S1. Table 2 lists all the focal mechanisms we obtain for the four sequences. We select the focal mechanisms of A and B quality for the following analysis. More information about the focal mechanism uncertainties can be found in the supplementary file.

To interpret the fault architecture for each sequence, we cluster the events based on focal mechanism similarity, which is measured as Kagan angle, defined as the rotation needed to bring two focal mechanisms into full alignment (Kagan, 1991). We compute the Kagan angle between all event pairs for each sequence and then apply a hierarchical clustering method in MATLAB to group the events, using a cutoff Kagan angle of 30°. Events in groups with fewer than five events are classified as unclustered events. For each group with similar focal mechanism, we use RANSAC method in MATLAB to fit a linear fault to the earthquake locations within this group.

### 3.4. Fault Stress State

After we obtain the focal mechanisms, we follow the approach used in the statewide analysis by Qin et al. (2019) to calculate the fault stress state for individual events. We use the regional stress field obtained by Qin et al. (2019) that the average principal stress amplitudes in Oklahoma are 30.0, 24.84, 15.46 MPa/km and the maximum horizontal principal stress orientations are 79°, 85°, 86°, 78°, for the Guthrie, Woodward, Cushing, and Fairview sequences, respectively. The events are projected onto 3D Mohr's Circles based on the strike and dip of focal mechanisms, and a normalized parameter *understress* (Gischig, 2015) is used to quantify the criticality of the fault plane. The understress is defined as:

$$understress = (\tau_p - \tau_0) / \tau_p \quad (3)$$

where $\tau_0$ is the shear stress on the fault calculated from the fault geometry and stress orientations, and $\tau_p$ is the shear stress at which slip initiates based on the Coulomb failure criterion under hydrostatic pore pressure. Since both $\tau_0$ and $\tau_p$ increase linearly with depth, the defined parameter understress is independent of depth (Qin et al., 2019). Values of understress near 0 imply that the faults are critically stressed, while values near one imply negligible resolved shear stress applied on the fault, and the fault is least favorably oriented. For each event, we calculate understress using both fault planes and select the one with lower understress as the real fault plane. We find that the focal mechanisms of a small number of earthquakes in the Woodward (10 events) and Fairview (2) sequences would require a pore pressure increase greater than the minimum principal stress (i.e., fracture opening) for rupture to occur. We suspect these are poorly constrained events due to relatively limited azimuthal coverage and so exclude them from the analysis.

## 4. Results

Using the techniques above, we obtain high-resolution earthquake relocations and 121, 137, 184, 414 high-quality focal mechanisms for Guthrie, Woodward, Cushing and Fairview sequences, respectively. The diffusive migration pattern of relocations is shown in Figure 2. The focal mechanisms and fault structures for each sequence are shown in Figures 3–6, with both map view and multiple cross-section views. Combining earthquake locations and understress values (Figure 7), we examine the spatial and temporal evolution of understress within individual fault zones (Figure 8). We first discuss the results for each sequence separately and then compare them to learn more about the driving mechanisms.

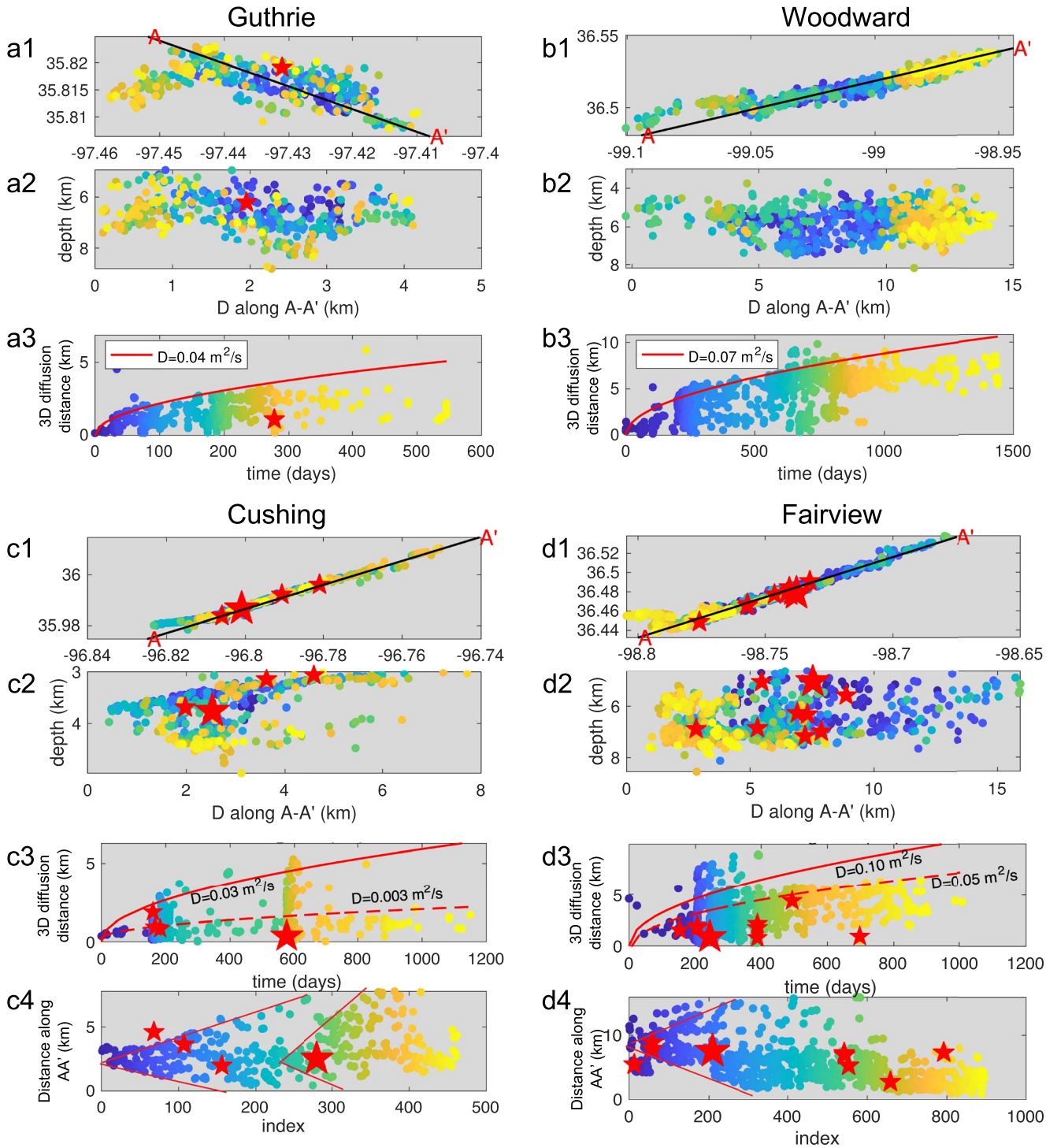


**Figure 2.** Migration patterns for four sequences. (a1) Map view of seismicity distribution in Guthrie sequence. The events are colored by the elapsed time from the first event in the sequence. Red stars are $M \geq 4.0$ earthquakes. (a2) Cross-section ($AA'$) view. (a3) The hypocentral distance from the average location of first 5% earthquakes of the sequence as a function of elapsed time in days. The red line is the best-fitted diffusion curve. The events are colored the same way as (a1, a2). (b1–b3) The same as (a1–a3) for Woodward sequence. (c1–c3) The same as (a1–a3) for Cushing sequence. (c4) Distance along Cushing main fault strike $AA'$ as a function of event index. The red lines are predicted linear growth of the rupture front with increasing event index. (d1–d3) The same as (a1–a3) for Fairview sequence. (d4) Distance along Fairview main fault strike $AA'$ as a function of event index. The red line is predicted linear growth of the rupture front with increasing event index.

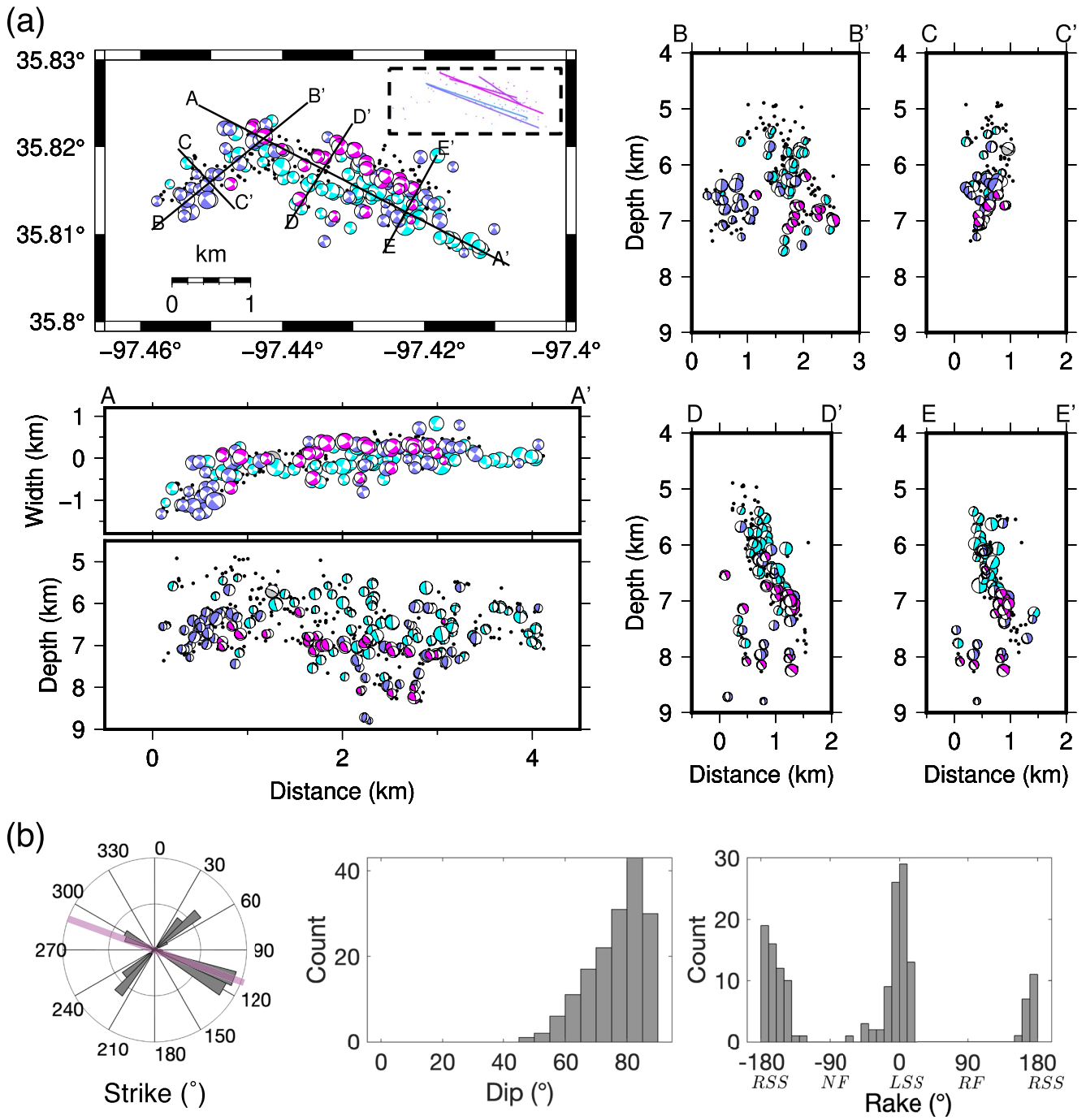


**Figure 3.** Earthquake relocations and focal mechanism solutions for Guthrie sequence. Subfigures (a) show the map view and cross-section views of the relocations (black dots) and focal mechanism solutions (beach balls). Each cross-section includes events within 1 km of the profile. Each color represents a cluster of events with similar focal mechanisms (cyan color denotes groups with similar fault planes to the largest event in the sequence, while pink denotes groups with largest difference from the largest event). Gray color represents unclustered events. The inset figure in the map view plot shows the interpreted fault structures. Both the interpreted faults and their corresponding focal mechanism groups are plotted using the same color scheme. Subfigures (b) show the histogram of strike, dip, and rake angles of focal mechanisms for Guthrie sequence. The magenta line on strike rose plot represents the orientation of main fault mapped from seismicity distribution. On the *x* axis of rake histogram, the faulting types are denoted below the rake angle. RSS: right-lateral strike-slip; NF: normal faulting; LSS: left-lateral strike-slip; RF: reverse faulting.

### 4.1. Guthrie ($M_{max}$ 4.3)

The Guthrie sequence is one of the earliest reactivated sequences in Oklahoma (e.g., Benz et al., 2015; McNamara et al., 2015; Schoenball et al., 2018). Figure 2a shows that the fault is initially reactivated at a depth of around

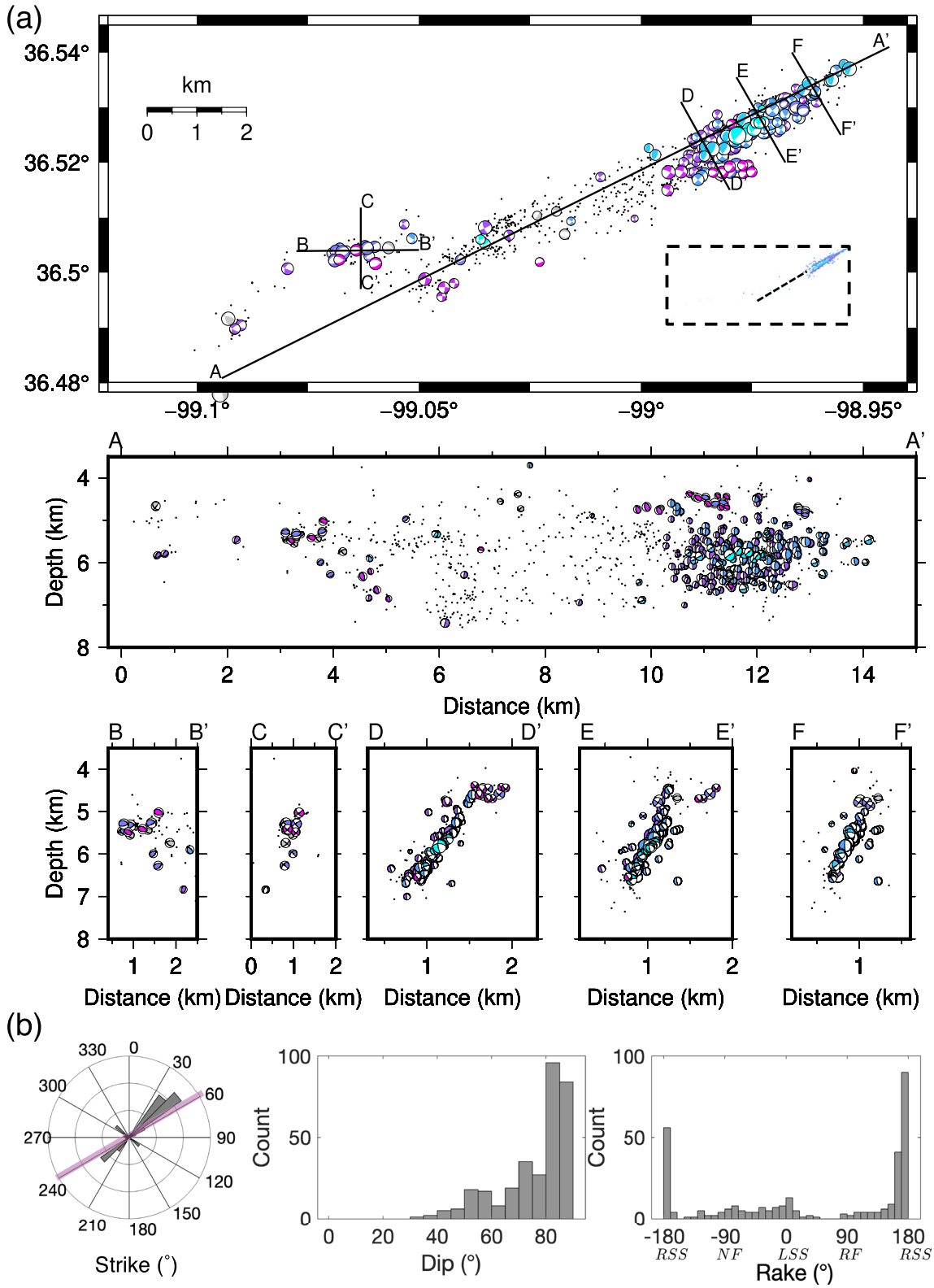


**Figure 4.**

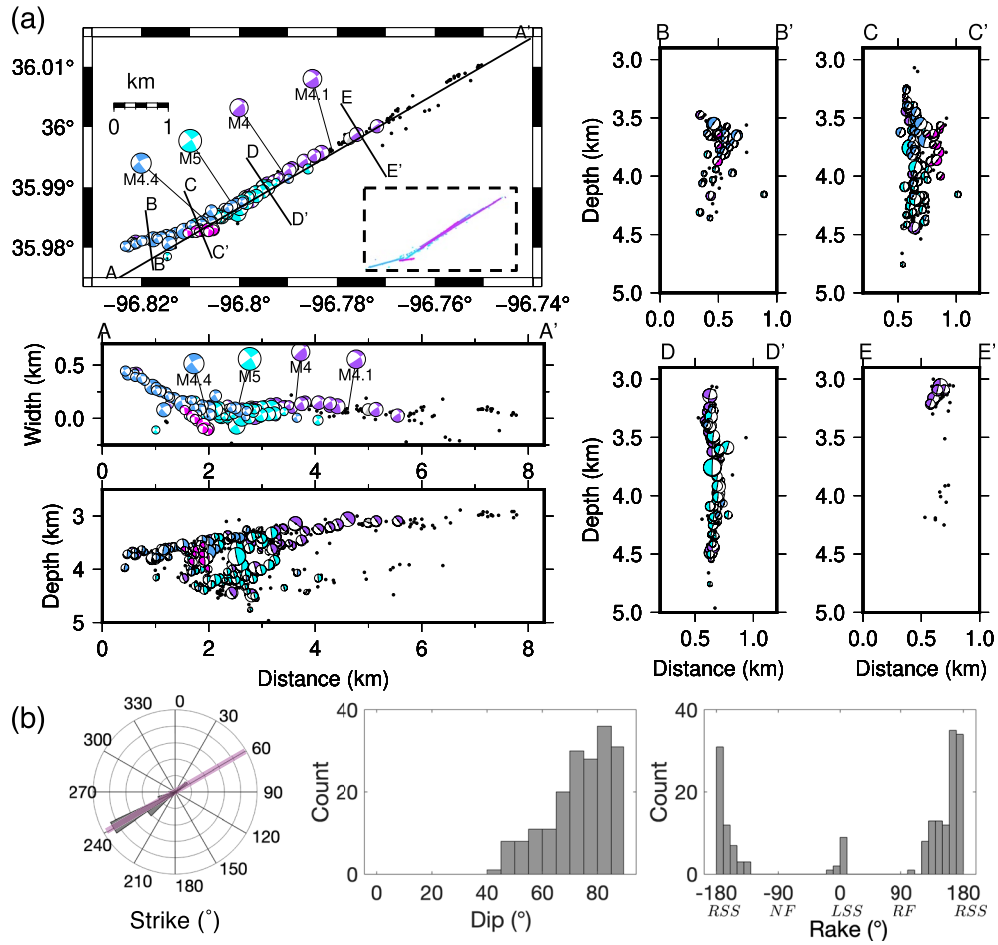


**Figure 5.** Earthquake relocations and focal mechanism solutions for Cushing sequence. (a) Map view and cross-section views of the relocation (black dots) and focal mechanism solutions (beach balls). The inset figure in the map view plot shows the interpreted fault structures. The color scheme is the same as Figure 3. (b) Histograms of strike, dip, and rake angles of focal mechanisms for Cushing sequence. The magenta line on strike rose plot represents the orientation of main fault mapped from seismicity distribution. On the *x* axis of rake histogram, the faulting types are denoted below the rake angle. RSS: right-lateral strike-slip; NF: normal faulting; LSS: left-lateral strike-slip; RF: reverse faulting.

6 km, and the seismicity exhibits continuous spatial migration away from the initiation point with a diffusivity of 0.04 $m^2/s$. The secondary structure to the southwest of the main fault is activated later in the sequence. The largest M4 event occurs near to the starting point of the sequence about 300 days following fault activation and ruptures a region where there had been a gap in the earlier seismicity (Pennington et al., 2022).

Using the focal mechanism clustering, we are able to map the detailed fault structure. Figure 3a shows a complicated fault mesh network with several fault segments, defining a diffuse fault zone. The NW trending main fault is vertical at shallow depths (<6.5 km) and dips to the northeast at greater depths. The vertical segment and the north dipping segment can be easily identified by different clusters of focal mechanisms, that is, vertical strike-slip events and dipping strike-slip events (cyan versus pink/purple colors in Profiles A-A′, D-D′, and E-E′). At the northwestern end of the main fault, a secondary northeast trending fault intersects with the main fault, which forms a conjugate fault pattern. Profile C-C′ crosses the secondary fault and shows that the secondary

**Figure 4.** Earthquake relocations and focal mechanism solutions for Woodward sequence. Subfigures (a) show the map view and cross-section views of the relocations (black dots) and focal mechanism solutions (beach balls). The inset figure in the map view plot shows the interpreted fault structures. The dashed black line is the inferred fault trend due to the lack of focal mechanisms in the central and southwest part of the main fault. The color scheme is the same as Figure 3. Subfigures (b) show the histogram of strike, dip, and rake angles of focal mechanisms for Woodward sequence. The magenta line on strike rose plot represents the orientation of main fault mapped from seismicity distribution. On the *x* axis of rake histogram, the faulting types are denoted below the rake angle. RSS: right-lateral strike-slip; NF: normal faulting; LSS: left-lateral strike-slip; RF: reverse faulting.

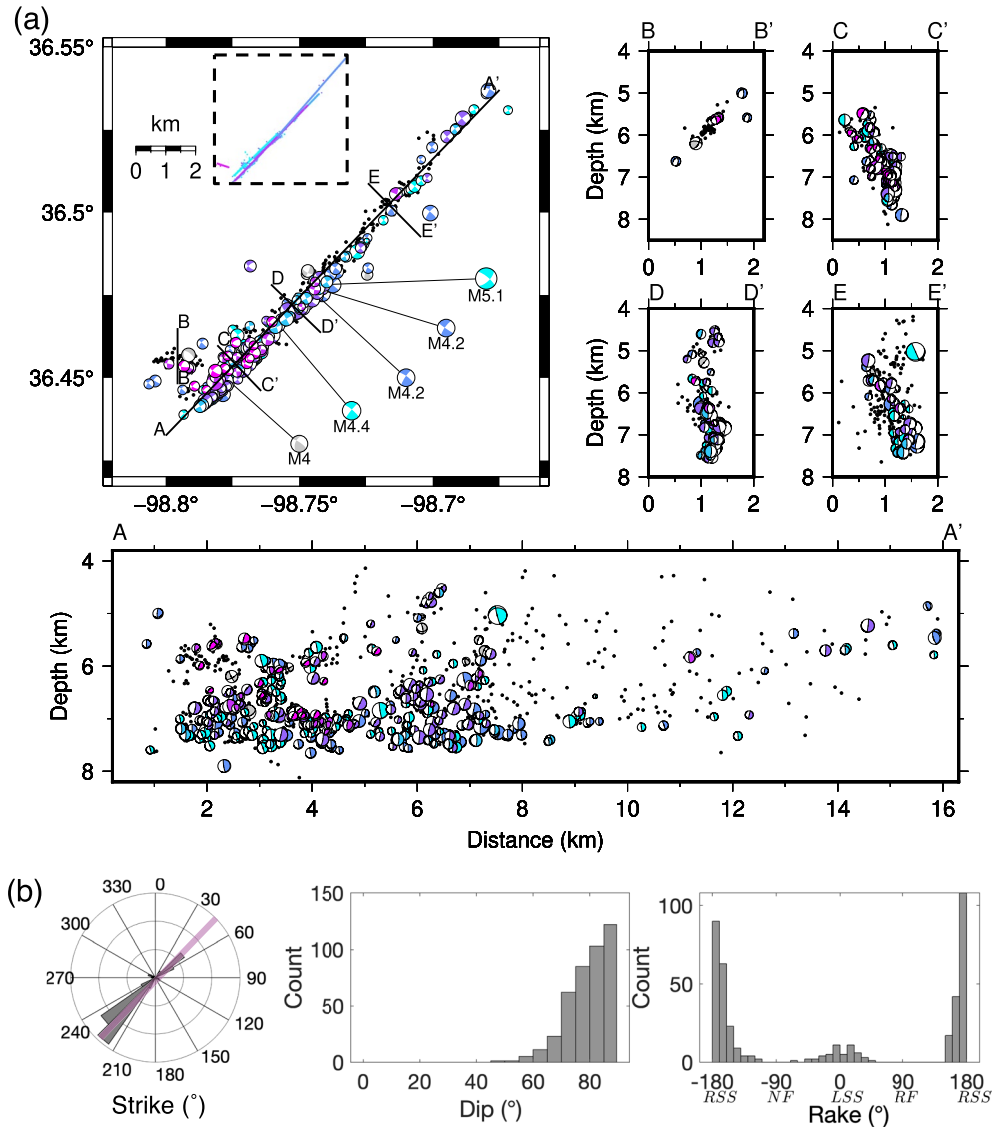


**Figure 6.** Earthquake relocations and focal mechanism solutions for Fairview sequence. Subfigures (a) show the map view and cross-section views of the relocations (black dots) and focal mechanism solutions (beach balls). The inset figure in the map view plot shows the interpreted fault structures. The color scheme is the same as Figure 3. Subfigures (b) show the histogram of strike, dip, and rake angles of focal mechanisms for Fairview sequence. The magenta line on strike rose plot represents the orientation of main fault mapped from seismicity distribution. On the *x* axis of rake histogram, the faulting types are denoted below the rake angle. RSS: right-lateral strike-slip; NF: normal faulting; LSS: left-lateral strike-slip; RF: reverse faulting.

fault dips 87° to the northwest direction. Interestingly, the events on the secondary fault show the same focal mechanisms as deep events on the main fault (purple color in Profile A-A′), suggesting similar stress regime on the two fault segments.

Figure 3b shows that the majority of the optimally oriented nodal planes have strike angle in the conjugate pattern of 110–130° and 210–240°, consistent with the conjugate fault pattern mapped from earthquake relocation. Most of the events are strike-slip events with dip angles varying from 45° to 90°.

Figure 7 shows the stress state using Mohr's Circles. Most of the events are optimally oriented, and the average understress for the sequence is 0.14. Fault activation begins at shallow depth on the main fault and propagates to increasing depth. The shallow events are slightly more optimally oriented than the deeper events (Figure 8a). Following the M4 earthquake in April 2015, there is a significant reduction in the injection rate (Chen et al., 2018).

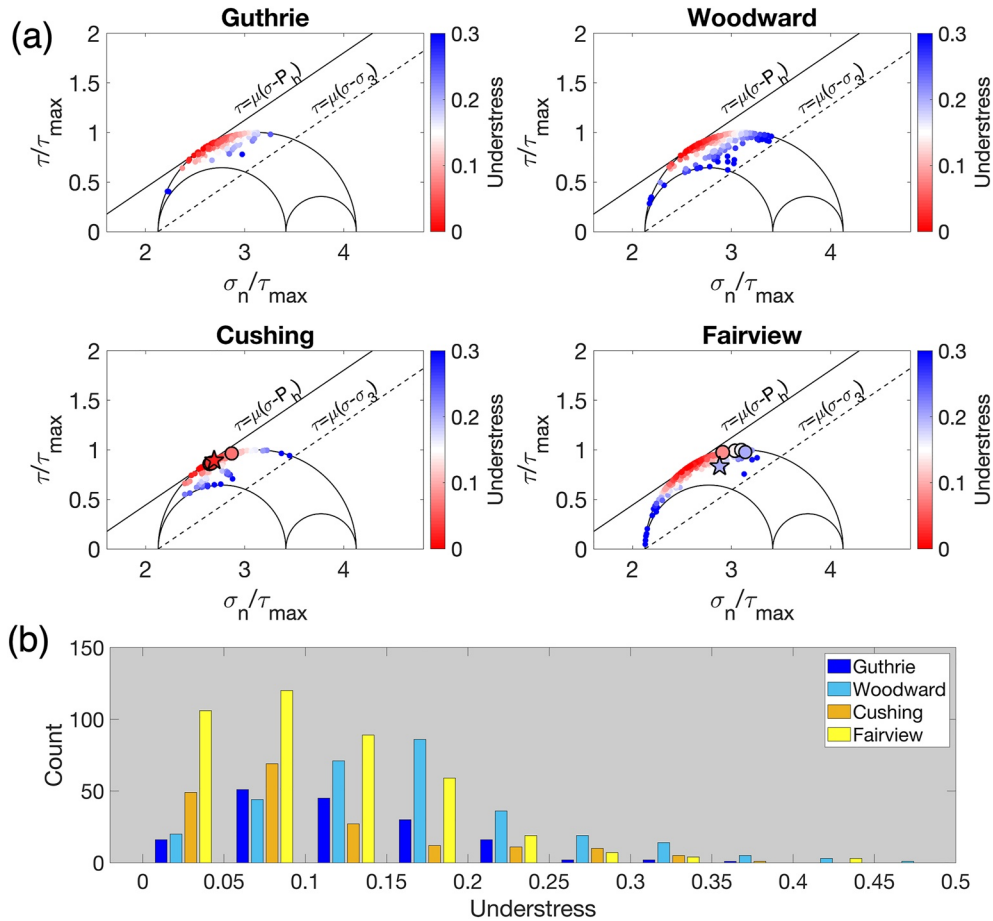


**Figure 7.** (a) The stress state of individual events in Guthrie, Woodward, Cushing, and Fairview sequences shown in 3D Mohr's Circle. The three semicircles represent the stress tensor, and the two straight lines represent the fault strength under hydrostatic fluid pressure and lithostatic pressure assuming a friction coefficient of 0.68. (b) The histogram of event understress for four sequences.

We observe a corresponding gradual decrease of understress value, suggesting that only the optimally oriented segments remain active following a decrease in pore pressure.

### 4.2. Woodward ($M_{max}$ 3.9)

Figure 2b shows that the entire sequence is well explained by fluid diffusion with best fitting diffusivity of 0.07 $m^2/s$ with multiple fault segments. The spatial migration is mostly continuous in time. Due to limited station coverage, the focal mechanisms of earliest earthquakes are not well resolved, therefore, we restrict our interpretation of the fault geometry and stress state evolution to the later seismicity in the sequence.

Figure 4b shows that the strike of individual fault planes is mostly within [30, 60]°. The individual fault plane solutions slightly differ from the main fault orientation mapped from seismicity relocation (N64°E) (magenta line in the rose diagram), suggesting complex fault zone structure. Most of the events are dipping steeply except a small subset of the events with dip angles between 40° and 70°. The dominant fault type is strike-slip faulting, but the sequence also hosts a small number of normal/oblique-normal faults (rake angle around −90°). Consistent with previous results Qin et al. (2018), the new focal mechanism results reflect an extensional stress regime at shallower depth.

In Figure 4a, the main fault is subvertical and dipping to northeast (D-D′, E-E′, F-F′). The events are mainly distributed at depth of 4–7 km. We identify four main clusters of focal mechanisms on the main fault (A-A′). First, there are two large clusters of vertical strike-slip events with different strike orientations covering the whole

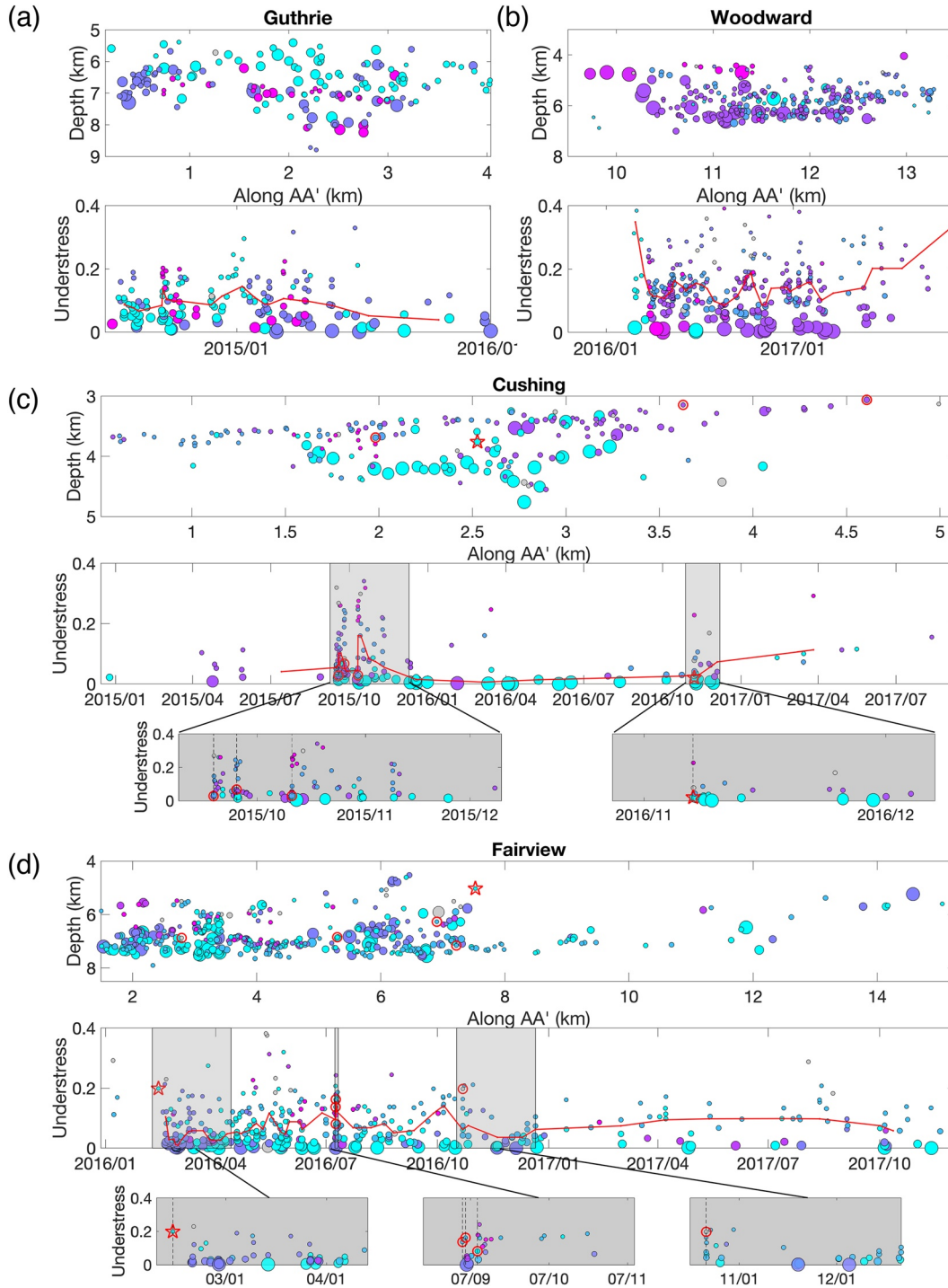


**Figure 8.** The temporal evolution of stress state in (a) Guthrie, (b) Woodward, (c) Cushing, and (d) Fairview sequences. For each sequence, the top panel shows the cross-section view plot along the main fault strike *AA′* (see Figures 3–6). The events are colored by the same color scheme in Figures 3–6. The points are inversely scaled by understress, that is, large points for critically stressed events, and vice versa. Red circles: $M \geq 4.0$; red stars: $M \geq 5.0$. The bottom panel shows the variations of stress state along time using the same color scheme as in Figures 3–6. The red line is the average understress over time. The shadow areas show the zoom in view around $M > 4$ events.

northeast area (blue and purple colors). This is evidence of fabrics of various orientations on the main fault plane. Second, a small group of dipping events occurred in the middle of the first two clusters (cyan colors), showing further complexity of the fault plane. Finally, we observe a splay of normal faulting events at shallow depth (around D-D′). To the west of the main fault, a shallow secondary fault segment is activated mainly with normal faulting events (Profiles B-B′ and C-C′).

The relatively scattered stress state distribution on the Mohr's Circles is consistent with the complexity of fault structure inferred from focal mechanism solutions (Figure 7b). The strike-slip events on the main fault are mostly optimally oriented, and the normal events at shallow depth are less optimally oriented. Figure 8b shows the spatial and temporal distribution of the stress state of individual faults in the Woodward sequence. The stress state is steady over time with only moderate variations. In space, the deeper events are significantly more critically stressed than shallow events.

### 4.3. Cushing ($M_{max}$ 5.0)

As shown in Figure 2c, the Cushing sequence initiates around the depth of 3.8 km in the middle of the fault zone, and the hypocenter location of the M5.0 event is nearly collocated with the earliest seismicity in the sequence (Figure 2c1). The radial expansion of the seismicity front follows a diffusion curve with best fitting diffusivity of 0.03 $m^2/s$ (Figure 2c2). However, the migration is discontinuous in time with two major seismicity bursts, the first burst with three $M \geq 4$ events (M4.1, M4, and M4.4), and the second burst with the M5.0 earthquake. In addition to the main migration front with diffusivity of 0.03 $m^2/s$, a background slower migration front with diffusivity of 0.003 $m^2/s$ is manually identified (dashed line in Figure 2c3). Although the temporal migration is discontinuous, the sequence exhibits continuous migration that can be characterized using an event index (Figure 2c4). The second burst following the M5.0 earthquake tends to expand faster than the first burst of activity characterized by multiple M4 earthquakes. Both these bursts of activity exhibit bilateral migration, with farther expansion toward the eastern end of the fault zone.

Figure 5 shows that the earthquakes define a narrow vertical fault zone (N60°E) with few secondary faults. The focal mechanism clustering results show four main groups (Profile A-A′). The first group including the M5.0 event is located within a seismicity gap in the middle of the wedge-shaped fault plane. The deeper events in the middle of the main fault share the same focal mechanism (near-vertical right-lateral strike-slip) as the M5.0. The second cluster is located in the northeast part of the main fault at slightly shallower depth and hosts two M4 events. Compared to the M5.0, the two events have more normal faulting component. The third group lies to the west end of the main fault and includes a secondary fault structure trending N76°E (Profile B-B′) depicted by a distinct group of focal mechanisms (blue color). Finally, Profile C-C′ crosses the intersection among the main fault, the secondary fault (Profile B-B′), and an EW-oriented left-lateral fault (pink color). The area shows considerable complexity and has a sharp change of faulting types.

The strikes of individual fault plane solutions in Cushing are largely coherent with the main fault strike inferred from seismicity (Figure 5b) and are mostly steeply dipping. Our previous study has shown that the Cushing fault is in a strike-slip faulting regime and the main fault is optimally oriented to the stress field (Qin et al., 2019). Under the regional stress field, all $M \geq 4$ events on the main fault are optimally oriented (Figure 7c). The cluster with M5.0 is more optimally oriented than other clusters. The fault activation begins with an optimally oriented segment near the center of the fault zone. Some nonoptimally oriented segments are activated after the M4 events during the first burst, including the left-lateral secondary fault (Figure 8c). Between the two bursts, most events occur along the optimally oriented main fault segment. The M5.0 event also activates a few nonoptimally oriented segments.

### 4.4. Fairview ($M_{max}$ 5.1)

Fairview sequence has one M5.1 earthquake in 2016 and numerous M4 earthquakes. The sequence is located near the edge of the seismic network coverage prior to the M5.1 earthquake in 2016, so some of the early earthquakes may have reduced accuracy of location and focal mechanism solutions. Figure 2d shows that most of the events follow diffusive migration pattern with a best fitting diffusivity of 0.10 $m^2/s$. However, a burst with two M4 earthquakes occurring prior to the M5.1 earthquake extends beyond the pressurized zone represented by the diffusion curve. Similar to the Cushing fault zone, a slower background diffusive migration front with a diffusivity of

0.05 $m^2/s$ can be manually identified. When examining distance along strike (profile A-A′) versus event index, we observe that the fault is activated with a small cluster in the middle and then propagates bilaterally, with the southwestern portion expanding more significantly and lasting over 300 days (Figures 2d3 and 2d4). The M5.1 event occurs about 200 days after fault activation and is within proximity to the initial fault activation location.

As shown in Figure 6a, the main fault in Fairview is a near-vertical fault with a strike of 44°. A secondary fault with a strike of 97° is inferred near the southern end of the main fault. The Fairview sequence has a dominant strike of 210–240°, and 89% of the fault planes have a dipping angle larger than 70° (Figure 6b).

Profile A-A′ in Figure 6a shows that there are two dense clusters of seismicity, one near the southern end (2–4 km along A-A′), and the other at 5–8 km where the M5.1 and several M4 events occurred. The two clusters have strike-slip faulting events with different dipping angles. Profile C-C′ crosses the first dense seismicity cluster near the southern end and shows a transition from a shallow dipping structure (mainly pink events in A-A′) to a deeper near-vertical structure at about 7 km. Profiles D-D′ crosses the second dense cluster near the center of the fault. There is a transition from a near-vertical dipping structure at shallow depth to a subvertical dipping structure at about 7 km depth. The fault narrows toward the northeastern end and has a few scattered strike-slip earthquakes at the northeastern end of the main fault (Profile E-E′). The depth extent changes from about 8 km near the southern end to about 6 km near the northern end. Different fault structures along strike (C-C′, D-D′, E-E′) show that the main fault is not a simple planar fault plane but with 3D variations. To the west of the main fault, there is a secondary, shallow dipping fault with narrow depth range, possibly a step-over connecting to the main fault (Profile B-B′).

The fault planes of M5.1 mainshock and a later M4 event are less optimally oriented. However, most small earthquake fault planes are optimally oriented, Figure 7d. Figure 8d shows the spatial and temporal distribution of the individual stress state in Fairview. In space, the events on the main faults are mostly optimally oriented except some shallow events. The Fairview sequence initiates later than the Woodward sequence, and the focal mechanism solutions cover most of the sequence except for the beginning before the M5.1 event. Therefore, we cannot determine the stress state of the fault segment at early fault activation stage.

## 5. Discussion

In this section, we combine all the findings, including fault structure, stress state, and pore pressure to probe the underlying triggering processes and evaluate the potential earthquake hazards.

### 5.1. Fault Architecture, Stress State, and Sequence Evolution

All four sequences show variations of focal mechanism solutions within individual fault zones and fluid-driven migration behavior in space and time with diffusivity values ranging from 0.03 to 0.1 $m^2/s$, consistent with the overall range reported in Haffener et al. (2018). Based on observations above, we can divide the sequences into two groups:

1. Guthrie and Woodward sequences occur on diffuse fault zones with several subparallel fault segments and a mixture of strike-slip dominated main fault and normal/oblique-normal secondary structures.

Both Guthrie and Woodward sequences show swarm-type evolution without clear mainshocks and continuous diffusive migration in time with similar diffusivities (Figure 2). Following the interpretation in Fischer and Hainzl (2021), these observations suggest Guthrie and Woodward sequences are dominated by fluid-driven external triggering process with limited earthquake interaction. The interpretation is consistent with previous observations. Chen et al. (2018) found that the Guthrie sequence showed strong temporal correlation between seismicity rate and injection rate from nearby disposal wells, suggesting fluid pressure dominated triggering process. Goebel et al. (2017) found that the Woodward fault zone was pressurized by both distant wells and a nearby disposal well through modeling.

2. Cushing and Fairview sequences occur on relatively narrow straight fault zones with the majority of small earthquakes on optimally oriented fault planes. Both sequences extend to deeper depth around the middle of the main fault zone where the $M \geq 5$ earthquakes occur. The depth extent gradually decreases toward the northeastern end of the faults, and fault width also narrows.

The Cushing mainshock fault plane is optimally oriented, while the Fairview mainshock fault plane is less optimally oriented. By comparing the cross-section views for Cushing and Fairview, we find that the width of fault zone (defined by the distance between the 20% and 80% of seismicity distribution in across-strike direction) in Fairview is larger than that in Cushing (~0.54 km versus ~0.12 km). The wider fault zone could explain the different fabric orientations from the main fault for the Fairview sequence.

For both sequences, there exists a slower, continuous background temporal migration (Figure 2 and 0.003 $m^2/s$ in Cushing and 0.05 $m^2/s$ in Fairview). Although both sequences exhibit some degree of bilateral expansion along strike, the Cushing sequence has more significant expansion toward northeast, while the Fairview sequence is more significant toward the southwest. Deng et al. (2020) found that the disposal well at the western end of the Cushing fault zone contributed largest pore pressure change within the fault zone. Moreover, all mapped seismicity on Cushing fault occurred within areas of positive Coulomb stress change from the injection wells. Yeck et al. (2016) and Goebel et al. (2017) attributed the triggering of the Fairview sequence to distant high-rate injection wells to the northeast of the sequence. Therefore, both Fairview and Cushing sequences show more significant spatial expansion away from disposal wells, consistent with long-term pore pressure propagation as underlying triggering mechanism.

Despite of the overall statistically significant diffusive migration, both Cushing and Fairview sequences exhibit some complexities in temporal migration. The most striking features on the migration curve are earthquake bursts beyond the slow pressure front. Cushing has two short-term earthquake bursts with larger events (e.g., $M \geq 4$) that cause discontinuous temporal migration. In Fairview, the earthquake burst at day 200 since fault activation disrupts the diffusive migration front. Similarly, on the migration with event index plot, both sequences show continuous migration. Based on Fischer and Hainzl (2021), Fairview and Cushing are more influenced by earthquake self-driven rupture growth. These differences can also be reflected from the coefficient of variation of interevent delay time ($C_v$) for each sequence (Cochran et al., 2018; Schoenball & Ellsworth, 2017a). The Guthrie and Woodward have relatively low $C_v$ values of 2.9 and 2.2, respectively, while Cushing and Fairview have larger $C_v$ values of 4.6 and 4.7, respectively, indicating higher degree of stress interactions during the two sequences with $M \geq 5$ earthquakes.

### 5.2. Interplay Between Fluid and Earthquake Rupture

The spatiotemporal evolution of earthquake sequences reflects the underlying driving forces. Chen et al. (2012) analyzed crustal earthquake bursts in Southern California and distinguished slow-slip driven, fluid driven, and aftershock-like bursts based on spatiotemporal migration patterns. The study also noted that diffusive migrating bursts were more likely to be associated with normal faulting events in southern California. The diffusivities found in Southern California mostly ranged from 0.01 to 0.16 $m^2/s$, which were similar to the observations in Oklahoma (Haffener et al., 2018), suggesting similar hydraulic properties of seismogenic faults in the crystalline basement. Fischer and Hainzl (2021) examined both earthquake spatial migration with time and with event index to understand cluster growth. In the traditional analysis of spatial migration with time, it assumes that earthquakes are passively responding to the spatial extent of external stress perturbation. However, earthquakes rupture can dynamically change the stress and permeability at rupture front (Yamashita, 1999). Therefore, there is dynamic feedback between external forcing and earthquake rupture process.

In fluid-rich environment, Yamashita (1999) performed numerical modeling to investigate the effect of pore creation on sequence evolution. The results showed that newly created fault slip would reduce pore pressure, creating a strengthening zone at the rupture front of an earthquake. If the pore creation speed was fast enough, no mainshock-aftershock could occur. Zhu et al. (2020) also quantified fault valving through 2-D antiplane shear simulations of earthquake sequences and found that fluid overpressure developed when healing/sealing reduced fault permeability and was released after earthquakes enhanced permeability. This dynamic interaction process among rupture, permeability, and fluid pressure can help further understand the influence of fault architecture on the sequence evolution observed here.

In the diffuse fault zones with multiple subparallel faults, such as Guthrie and Woodward, the wide fault zones are highly fractured (Figure 2). In Guthrie and Woodward, both sequences host a significant fraction of normal faulting events. Sibson (1993) showed that normal faulting always experienced loading-weakening, while strike-slip faulting could be either loading-weakening or loading-strengthening depending on the stress field. The

loading-weakening means that fault strength decreases with increasing shear stress. Both the wide fractured zones and the loading-weakening behavior could facilitate crack opening and fast pore creation, preventing nucleation of large mainshock-aftershock bursts and leading to more continuous temporal migration.

Within the Cushing fault zone, two apparent diffusive migration fronts are identified: one slower front for background seismicity, and one faster front enclosing the two seismicity bursts (Figure 2c3). It is likely that the rupture from larger events enhances the fault zone permeability, generating a faster migration front during the earthquake bursts. This is similar to the fault valve behavior (Sibson, 1981), where the earthquake rupture creates fluid pathways and provides a conduit for high-pressure fluid. Many swarm migrations have been attributed to the fault valve behavior, for example, Shelly et al. (2015); Ruhl et al. (2016); Ross et al. (2020). The Fairview fault zone exhibits similar but less evident behavior compared to the Cushing fault zone (Figure 2d3). In these two sequences, earthquake rupture is the main factor that drives the cluster growth based on the migration pattern with event index. However, the role of fluid is also crucial. The pressure drop from the enhanced permeability structure likely limits the rupture extent of each burst and the nucleation of the largest events. For both sequences, the hypocenters of the $M \geq 5$ events are within proximity to the location of fault activation (earliest earthquakes in the sequence), implying that the initial pressurized zone may lead to the nucleation of the largest event (Figures 2c3 and 2d3). The more significant spatial expansion in the direction away from high-rate injection wells for both sequences suggests that long-term pore pressure propagation in the subsurface continues to influence earthquake occurrence (Figures 2c4 and 2d4).

These observations suggest that fault architecture influences sequence evolution and dominant driving forces for induced seismicity, which provides an analogy to other fluid driven earthquake swarms. Ruhl et al. (2016) mapped complex fault-fracture mesh and identified an individual sequence matching the fault valve behavior. Shelly, Ellsworth, and Hill (2016) found that during the 2014 Long Valley Caldera, California earthquake swarm, different fault structures affected the degree of fluid confinement within a fault zone and the subsequent earthquake hypocenters and sequence $b$ values. Ross et al. (2020) observed that the fault in Cahuilla swarm, California was divided into two sections by permeability barrier and the changing permeability affected the earthquake migration pattern. We did not observe significant updip migration in the four sequences. Instead, the major migration pattern is in horizontal direction along the main fault strike. However, similar to other swarms, the fault structure influences the fluid distribution and controls the sequence evolution.

## 6. Conclusions

We determine high-resolution relocations and focal mechanism solutions for small earthquakes within four sequences in Oklahoma. We map detailed fault architecture and stress state evolution using focal mechanisms. We integrate the earthquake relocation with the spatiotemporal migration and fault architectures and find that the entire behavior of the sequences can be related to the orientation and geometry of the fault structures in the stress field.

In Cushing and Fairview, the narrow, simpler strike-slip dominated fault zones promote burst-like behaviors with larger events (e.g., $M \geq 5$), where earthquake rupture-driven spatial expansion dominates. However, in Guthrie and Woodward, the more complex and diffuse fault zones with a mixture of strike-slip and normal faulting events host swarm-type sequences ($M < 5$) with continuous temporal diffusive migration, where fluid driven triggering process dominates.

Besides the first-order observation in Cushing and Fairview, we also observe fluid-faulting interactions. The overall spatial expansion direction is consistent with pore pressure diffusion away from high-rate injection wells, suggesting pressure change continues to operate in the background. Evidence shows that earthquake rupture may have enhanced diffusivity in the surrounding rock matrix, leading to faster spatial expansion during bursts with larger earthquakes.

## Data Availability Statement

All seismic data were downloaded through the IRIS Wilber 3 system (https://ds.iris.edu/wilber3/) or IRIS Web Services (https://service.iris.edu/), including the following seismic networks: (a) the GS (Albuquerque Seismological Laboratory (ASL)/USGS, 1980); (b) the N4 (Albuquerque Seismological Laboratory (ASL)/USGS, 2013);

(c) the NQ (U.S. Geological Survey, 1989); (d) the NX (Nanometrics Seismological Instruments, 2013); (e) the OK (Oklahoma Geological Survey, 1978); (f) the O2 (Oklahoma Geological Survey, 2018); (g) the TA (IRIS Transportable Array, 2003); (h) the US (Albuquerque Seismological Laboratory (ASL)/USGS, 1990); (i) the YW (Anderson et al., 2016); (j) the Y7 (Nori, 2016); (k) the Y9 (Chen et al., 2016); (l) the ZD (Darold, 2014); (m) the ZP (Chang, 2016).

**Acknowledgments**
Y. Q. and X. C. were partially supported by USGS NEHRP Grant G18AP00022 and NSF award 2043064 to the University of Oklahoma. Y. Q. and T. C. are supported by the U.S. Department of Energy (DOE) Office of Fossil Energy and Carbon Management through award LANL-19-FE-1122-19-FY20. R. E. A. is supported by NSF award 2043281 to Boston University. We thank the Oklahoma Geological Survey for providing earthquake data (https://ogsweb.ou.edu/eq_catalog/). We are grateful for the constructive comments of two anonymous reviewers, the Associate Editor and the Editor Satoshi Ide, whose suggestions improved the quality and clarity of the manuscript.

## References

Albuquerque Seismological Laboratory (ASL), USGS. (1980). *US geological survey networks*. International Federation of Digital Seismograph Networks. https://doi.org/10.7914/SN/GS

Albuquerque Seismological Laboratory (ASL), USGS. (1990). *United States national seismic network*. International Federation of Digital Seismograph Networks. https://doi.org/10.7914/SN/US

Albuquerque Seismological Laboratory (Asl), USGS. (2013). *Central and eastern US network*. International Federation of Digital Seismograph Networks. https://doi.org/10.7914/SN/N4

Anderson, K., Sweet, J., & Woodward, B. (2016). *Iris community wavefield experiment in Oklahoma*. International Federation of Digital Seismograph Networks. https://doi.org/10.7914/SN/YW_2016

Benz, H. M., McMahon, N. D., Aster, R. C., McNamara, D. E., & Harris, D. B. (2015). Hundreds of earthquakes per day: The 2014 Guthrie, Oklahoma, earthquake sequence. *Seismological Research Letters*, *86*(5), 1318–1325. https://doi.org/10.1785/0220150019

Chang, J. (2016). *Seismic investigation of south central Oklahoma*. International Federation of Digital Seismograph Networks. https://doi.org/10.7914/SN/ZP_2016

Chen, X., Haffener, J., Goebel, T. H., Meng, X., Peng, Z., & Chang, J. C. (2018). Temporal correlation between seismic moment and injection volume for an induced earthquake sequence in central Oklahoma. *Journal of Geophysical Research: Solid Earth*, *123*, 3047–3064. https://doi.org/10.1002/2017JB014694

Chen, X., Nakata, N., Pennington, C., Haffener, J., Chang, J. C., He, X., & Walter, J. I. (2017). The Pawnee earthquake as a result of the interplay among injection, faults and foreshocks. *Scientific Reports*, *7*(1), 1–18. https://doi.org/10.1038/s41598-017-04992-z

Chen, X., Peng, Z., Jefferson, C., & Chang. (2016). *Rapid response for Fairview aftershock in Oklahoma*. International Federation of Digital Seismograph Networks. https://doi.org/10.7914/SN/Y9_2016

Chen, X., Shearer, P. M., & Abercrombie, R. E. (2012). Spatial migration of earthquakes within seismic clusters in southern California: Evidence for fluid diffusion. *Journal of Geophysical Research*, *117*, B04301. https://doi.org/10.1029/2011JB008973

Cochran, E. S., Ross, Z. E., Harrington, R. M., Dougherty, S. L., & Rubinstein, J. L. (2018). Induced earthquake families reveal distinctive evolutionary patterns near disposal wells. *Journal of Geophysical Research: Solid Earth*, *123*, 8045–8055. https://doi.org/10.1029/2018JB016270

Darold, A. (2014). *4d integrated study using geology, geophysics, reservoir modeling rock mechanics to develop assessment models for potential-* International Federation of Digital Seismograph Networks. https://doi.org/10.7914/SN/ZD_2014

Darold, A. P., Holland, A. A., Morris, J. K., & Gibson, A. R. (2015). Oklahoma earthquake summary report 2014. (Okla. Geol. Surv. Open-File Rept. OF1-2015 pp. 1–46). Oklahoma Geological Survey.

De Matteis, R., Convertito, V., & Zollo, A. (2016). Bistrop: Bayesian inversion of spectral-level ratios and p-wave polarities for focal mechanism determination. *Seismological Research Letters*, *87*(4), 944–954. https://doi.org/10.1785/0220150259

Deng, K., Liu, Y., & Chen, X. (2020). Correlation between poroelastic stress perturbation and multidisposal wells induced Earthquake sequence in Cushing, Oklahoma. *Geophysical Research Letters*, *47*, e2020GL089366. https://doi.org/10.1029/2020GL089366

Ellsworth, W. L. (2013). Injection-induced earthquakes. *Science*, *341*(6142), 1225942. https://doi.org/10.1126/science.1225942

Fischer, T., & Hainzl, S. (2021). The growth of earthquake clusters. *Frontiers of Earth Science*, *9*, 1–13. https://doi.org/10.3389/feart.2021.638336

Gischig, V. S. (2015). Rupture propagation behavior and the largest possible earthquake induced by fluid injection into deep reservoirs. *Geophysical Research Letters*, *42*, 7420–7428. https://doi.org/10.1002/2015GL065072

Goebel, T., Weingarten, M., Chen, X., Haffener, J., & Brodsky, E. (2017). The 2016 Mw5.1 Fairview, Oklahoma earthquakes: Evidence for long-range poroelastic triggering at >40 km from fluid disposal wells. *Earth and Planetary Science Letters*, *472*, 50–61. https://doi.org/10.1016/j.epsl.2017.05.011

Haffener, J., Chen, X., & Murray, K. (2018). Multiscale analysis of spatiotemporal relationship between injection and seismicity in Oklahoma. *Journal of Geophysical Research: Solid Earth*, *123*, 8711–8731. https://doi.org/10.1029/2018JB015512

Hardebeck, J. L., & Shearer, P. M. (2008). Hash: A fortran program for computing earthquake first-motion focal mechanisms—v1. 2—January 31, 2008. Retrieved from https://www.usgs.gov/software/hash-12

IRIS Transportable Array. (2003). *USArray transportable array*. International Federation of Digital Seismograph Networks. https://doi.org/10.7914/SN/TA

Kagan, Y. (1991). 3-d Rotation of double-couple earthquake sources. *Geophysical Journal International*, *106*(3), 709–716. https://doi.org/10.1111/j.1365-246x.1991.tb06343.x

Keranen, K. M., Savage, H. M., Abers, G. A., & Cochran, E. S. (2013). Potentially induced earthquakes in Oklahoma, USA: Links between wastewater injection and the 2011 Mw 5.7 earthquake sequence. *Geology*, *41*(6), 699–702. https://doi.org/10.1130/G34045.1

Keranen, K. M., Weingarten, M., Abers, G. A., Bekins, B. A., & Ge, S. (2014). Sharp increase in central Oklahoma seismicity since 2008 induced by massive wastewater injection. *Science*, *345*(6195), 448–451. https://doi.org/10.1126/science.1255802

Kwiatek, G., Martínez-Garzón, P., & Bohnhoff, M. (2016). Hybridmt: A Matlab/shell environment package for seismic moment tensor inversion and refinement. *Seismological Research Letters*, *87*(4), 964–976. https://doi.org/10.1785/0220150251

Li, Z., & Peng, Z. (2016). An automatic phase picker for local earthquakes with predetermined locations: Combining a signal-to-noise ratio detector with 1d velocity model inversion. *Seismological Research Letters*, *87*(6), 1397–1405. https://doi.org/10.1785/0220160027

McGarr, A., & Barbour, A. J. (2017). Wastewater disposal and the earthquake sequences during 2016 near Fairview, Pawnee, and Cushing, Oklahoma. *Geophysical Research Letters*, *44*, 9330–9336. https://doi.org/10.1002/2017GL075258

McNamara, D. E., Benz, H. M., Herrmann, R. B., Bergman, E. A., Earle, P., Holland, A., et al. (2015). Earthquake hypocenters and focal mechanisms in central Oklahoma reveal a complex system of reactivated subsurface strike-slip faulting. *Geophysical Research Letters*, *42*, 2742–2749. https://doi.org/10.1002/2014GL062730

Nanometrics Seismological Instruments. (2013). *Nanometrics research network*. International Federation of Digital Seismograph Networks. https://doi.org/10.7914/SN/NX

Nakata, N. (2016). *Acquisition of aftershock sequence of the 2016 m5.6 sooner lake earthquake*. International Federation of Digital Seismograph Networks. https://doi.org/10.7914/SN/Y7_2016

Oklahoma Geological Survey. (1978). *Oklahoma seismic network*. International Federation of Digital Seismograph Networks. https://doi.org/10.7914/SN/OK

Oklahoma Geological Survey. (2018). *Oklahoma consolidated temporary seismic networks*. International Federation of Digital Seismograph Networks. https://doi.org/10.7914/SN/O2

Pennington, C., & Chen, X. (2017). Coulomb stress interactions during the Mw 5.8 Pawnee sequence. *Seismological Research Letters*, *88*(4), 1024–1031. https://doi.org/10.1785/0220170011

Pennington, C., Uchide, T., & Chen, X. (2022). Slip characteristics of induced earthquakes: Insights from the 2015 mw 4.0 Guthrie, Oklahoma earthquake. *Journal of Geophysical Research: Solid Earth*, *127*, e2021JB023564. 10.1029/2021JB023564

Pugh, D., White, R., & Christie, P. (2016). A Bayesian method for microseismic source inversion. *Geophysical Journal International*, *206*(2), 1009–1038. https://doi.org/10.1093/gji/ggw186

Qin, Y., Chen, X., Carpenter, B. M., & Kolawole, F. (2018). Coulomb stress transfer influences fault reactivation in areas of wastewater injection. *Geophysical Research Letters*, *45*, 11059–11097. https://doi.org/10.1029/2018GL79713

Qin, Y., Chen, X., Walter, J. I., Haffener, J., Trugman, D. T., Carpenter, B. M., et al. (2019). Deciphering the stress state of seismogenic faults in Oklahoma and southern Kansas based on an improved stress map. *Journal of Geophysical Research: Solid Earth*, *124*, 12920–12934. https://doi.org/10.1029/2019JB018377

Ross, Z. E., Cochran, E. S., Trugman, D. T., & Smith, J. D. (2020). 3d fault architecture controls the dynamism of earthquake swarms. *Science*, *368*(6497), 1357–1361. https://doi.org/10.1126/science.abb0779

Ross, Z. E., Meier, M.-A., & Hauksson, E. (2018). P wave arrival picking and first-motion polarity determination with deep learning. *Journal of Geophysical Research: Solid Earth*, *123*, 5120–5129. https://doi.org/10.1029/2017JB015251

Ruhl, C., Abercrombie, R., Smith, K., & Zaliapin, I. (2016). Complex spatiotemporal evolution of the 2008 mw 4.9 mogul earthquake swarm (reno, Nevada): Interplay of fluid and faulting. *Journal of Geophysical Research: Solid Earth*, *121*, 8196–8216. https://doi.org/10.1002/2016JB013399

Schoenball, M., & Ellsworth, W. L. (2017a). A systematic assessment of the spatiotemporal evolution of fault activation through induced seismicity in Oklahoma and southern Kansas. *Journal of Geophysical Research: Solid Earth*, *122*, 10189–10206. https://doi.org/10.1002/2017JB014850

Schoenball, M., & Ellsworth, W. L. (2017b). Waveform-relocated earthquake catalog for Oklahoma and southern Kansas illuminates the regional fault network. *Seismological Research Letters*, *88*(5), 1252–1258. https://doi.org/10.1785/0220170083

Schoenball, M., Walsh, F. R., Weingarten, M., & Ellsworth, W. L. (2018). How faults wake up: The Guthrie-Langston, Oklahoma earthquakes. *The Leading Edge*, *37*(2), 100–106. https://doi.org/10.1190/tle37020100.1

Shelly, D. R., Ellsworth, W. L., & Hill, D. P. (2016). Fluid-faulting evolution in high definition: Connecting fault structure and frequency-magnitude variations during the 2014 long valley caldera, California, earthquake swarm. *Journal of Geophysical Research: Solid Earth*, *121*, 1776–1795. https://doi.org/10.1002/2015JB012719

Shelly, D. R., Hardebeck, J. L., Ellsworth, W. L., & Hill, D. P. (2016). A new strategy for earthquake focal mechanisms using waveform-correlation-derived relative polarities and cluster analysis: Application to the 2014 long valley caldera earthquake swarm. *Journal of Geophysical Research: Solid Earth*, *121*, 8622–8641. https://doi.org/10.1002/2016JB013437

Shelly, D. R., Taira, T., Prejean, S. G., Hill, D. P., & Dreger, D. S. (2015). Fluid-faulting interactions: Fracture-mesh and fault-valve behavior in the february 2014 mammoth mountain, California, earthquake swarm. *Geophysical Research Letters*, *42*, 5803–5812. https://doi.org/10.1002/2015GL064325

Sibson, R. H. (1981). Fluid flow accompanying faulting: Field evidence and models. In *Earthquake prediction: An international review* (Vol. 4, pp. 593–603). American Geophysical Union.

Sibson, R. H. (1993). Load-strengthening versus load-weakening faulting. *Journal of Structural Geology*, *15*, 123–128. https://doi.org/10.1016/0191-8141(93)90090-w

Skoumal, R. J., Kaven, J. O., & Walter, J. I. (2019). Characterizing seismogenic fault structures in Oklahoma using a relocated template-matched catalog. *Seismological Research Letters*, *90*(4), 1535–1543. https://doi.org/10.1785/0220190045

U.S. Geological Survey. (1989). *Netquakes*. International Federation of Digital Seismograph networks. https://doi.org/10.7914/SN/NQ

Vavryčuk, V. (2015). Inversion for the composite moment tensor. *Bulletin of the Seismological Society of America*, *105*(6), 3024–3035.

Waldhauser, F. (2001). hypodd—A program to compute double-difference hypocenter locations (hypodd version 1.0-03/2001. *US Geol. Surv. Open File Rep.*, 01, 113).

Walter, J. I., Ogwari, P., Thiel, A., Ferrer, F., Woelfel, I., Chang, J. C., et al. (2020). The Oklahoma geological survey statewide seismic network. *Seismological Research Letters*, *91*(2A), 611–621. https://doi.org/10.1785/0220190211

Wu, Q., Chen, X., & Abercrombie, R. E. (2019). Source complexity of the 2015 mw 4.0 Guthrie, Oklahoma earthquake. *Geophysical Research Letters*, *46*, 4674–4684. https://doi.org/10.1029/2019GL082690

Yamashita, T. (1999). Pore creation due to fault slip in a fluid-permeated fault zone and its effect on seismicity: Generation mechanism of earthquake swarm. *Pure and Applied Geophysics*, *155*, 625–647. https://doi.org/10.1007/s000240050280

Yeck, W. L., Weingarten, M., Benz, H. M., McNamara, D. E., Bergman, E., Herrmann, R., et al. (2016). Far-field pressurization likely caused one of the largest injection induced earthquakes by reactivating a large preexisting basement fault structure. *Geophysical Research Letters*, *43*, 10–198. https://doi.org/10.1002/2016GL070861

Zhu, W., Allison, K. L., Dunham, E. M., & Yang, Y. (2020). Fault valving and pore pressure evolution in simulations of earthquake sequences and aseismic slip. *Nature Communications*, *11*(1), 1–11. https://doi.org/10.1038/s41467-020-18598-z